mathematics

MDPI

Article

Generation and Controllability of High-Dimensional Rogue Waves in an Electromagnetically Induced Transparent Medium

Zhongyin Li [1,2], Ji Lin [2] and Huijun Li [2,*]

[1] Institute of Mathematics and Physics and School of Arts and Sciences, Nanning College of Technology, Guilin 541006, China
[2] Department of Physics, Institute of Nonlinear Physics, Zhejiang Normal University, Jinhua 321004, China
* Correspondence: hjli@zjnu.cn

Abstract: We propose a scheme to generate and control high-dimensional rogue waves in a coherent three-level Λ-type atomic system via electromagnetically induced transparency (EIT). Under EIT conditions, the probe field envelopes obey the non-integrable nonlinear Schrödinger equations (NLSE) with or without the external potential, which result from the stark (Zeeman) effect contributed by an electric (magnetic) field. By adjusting the amplitude and width of the initial pulse, we can generate the high-dimensional rogue waves and obtain the phase-transition curves of high-dimensional rogue waves. In the system, the far-detuned electric field, the random weak magnetic field, and the Gauss weak magnetic field are not conducive to the excitation of high-dimensional rogue waves. The results not only provide a theoretical basis for the experimental realization or prevention of the high-dimensional rogue waves, but also prove the possibility of generating and controlling the rogue waves in other high-dimensional non-integrable systems.

Keywords: rogue waves; electromagnetically induced transparent; non-integrable systems

MSC: 81P40; 81V10

Citation: Li, Z.; Lin, J.; Li, H. Generation and Controllability of High-Dimensional Rogue Waves in an Electromagnetically Induced Transparent Medium. *Mathematics* **2023**, *11*, 1829. https://doi.org/10.3390/math11081829

Academic Editor: Dmitry Makarov

Received: 11 February 2023
Revised: 1 April 2023
Accepted: 10 April 2023
Published: 12 April 2023

1. Introduction

Rogue waves, first detected in the ocean [1–3], are extreme local waves [4–10]. They could devour ships in the ocean as they sail. Draper, a British scientist, first proposed the concept of the freak wave in the scientific literature in 1965 [11], and it has since attracted the attention of researchers in the field of nonlinear optics. Since the United States ship Ramapo was hit by an extreme shock wave [1], rogue waves in the ocean have caused many catastrophic events [12–16]. Therefore, it is necessary to understand the characteristics of the rogue wave and to obtain the mechanism of its regulation. On the one hand, rogue waves have localization of time and space [4,5]. On the other hand, the peak height of the rogue wave is at least 2.2 times higher than the background plane value [6,7,17,18]. In the past few decades, the research progress of rogue waves was slow. In 2007, Solli et al. first observed rogue waves experimentally [19], and in 2010, Kibler et al. observed Peregrine solitons [20] through a combination of experiment and numerical simulations. These two works have made the study of rogue waves a hot topic. There have also been many reports of rogue waves in recent years [21–45].

In the past thirty years, the phenomena and applications of weak-light nonlinear optics have attracted much attention, especially electromagnetic induced transparency (EIT), which is an ideal platform for studying the nonlinear effects of weak light. Currently, there are many reports about EIT [46–52]. There are also reports about analytic solitons [53], dark solitons [54], and spatial solitons [55]. On the one hand, it can significantly enhance nonlinearity [56], inhibit absorption [57], and reduce group velocity [58]. On the other hand, parameters such as control field, detunings, and density with atoms can be regulated [59]. These advantages make it an ideal platform for studying

nonlinear phenomena, especially rogue waves [17,60,61]. Recently, in the EIT system, one-dimensional analytic [60,61] and numerical [17] rogue waves of integrable model have been discussed. However, the high-dimensional rogue waves of non-integrable model have not been reported yet.

In this paper, we consider a resonant, three-level, Λ-type EIT system. The high-dimensional envelope equation satisfied by the probe field is obtained. By taking the different initial parameters and external electric or magnetic fields, the different nonlinear Schrödinger equations (NLSE) are obtained, including the high-dimensional Kerr NLSE, the high-dimensional, non-integrable, saturated, nonlinear Schrödinger equation (SNLSE) and the high-dimensional, non-integrable SNLSE with external potential. By adjusting the amplitude and width of the initial pulse, we not only obtain the high-dimensional rogue waves, but also get the phase-transition curves between rogue wave and general wave. We find that the far-detuned electric field, the random weak magnetic field, and the Gauss weak magnetic field are not conducive to the excitation of high-dimensional rogue waves, so the external fields can be used to inhibit the excitation of high-dimensional rogue waves, prevent and control the high-dimensional rogue waves. There are three contributions of this article. Firstly, we obtain the rogue-wave solutions of three kinds of models under different conditions. Secondly, we provide a universal method for studying the rogue-wave solutions of non-integrable nonlinear models. Finally, it provides a scheme to control rogue waves through electric and magnetic fields.

2. Model

We consider a lifetime-broadened atomic system with a Λ-type energy-level configuration, as shown in Figure 1. A weak probe field $\mathbf{E}_p = \mathbf{e}_x \mathcal{E}_p(x,y,z,t) \exp\left[i(k_p z - \omega_p t)\right] + \text{c.c.}$ and a strong control field $\mathbf{E}_c = \mathbf{e}_x \mathcal{E}_c \exp\left[i(-k_c z - \omega_c t)\right] + \text{c.c.}$ interact resonantly with levels $|1\rangle \to |3\rangle$ and $|2\rangle \to |3\rangle$, respectively. Here, $\mathbf{e}_j$, k_j, and $\mathcal{E}_j$, are the polarization unit vector in the jth direction, the wave number, and the envelope of the jth field, respectively. The levels $|l\rangle$ $(l = 1,2,3)$, together with $\mathbf{E}_p$ and $\mathbf{E}_c$, constitute a well-known Λ-type EIT core in which the absorption of probe field is suppressed due to the quantum interference effect induced by the control field.

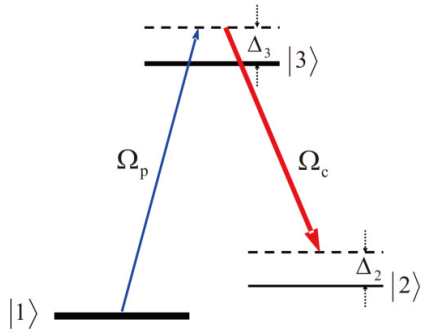

Figure 1. (Color online) Excitation scheme of the lifetime broadened three-state atomic system interacting with a weak probe field with the half Rabi frequency Ω_p, and a strong continuous-wave control field with the half Rabi frequency Ω_c.

Furthermore, a far-detuned (Stark) optical lattice field $\mathbf{E}_{\text{Stark}} = \mathbf{e}_y \sqrt{2} E_0(x,y) \cos(\omega_L t)$ and a weak magnetic field $\mathbf{B}(x,y) = \mathbf{e}_y B_1(x,y)$ are added to the system, where E_0 and ω_L are the field amplitude and angular frequency, respectively; $B_1(x,y)$ is a nonuniform magnetic field distributed in the transverse direction. Due to the existence of $\mathbf{E}_{\text{Stark}}$ and $\mathbf{B}(x,y)$, a small Stark shift $\Delta E_j = -\frac{1}{2}\alpha_j \langle \mathbf{E}^2_{\text{Stark}} \rangle_t = -\frac{1}{2}\alpha_j E_0^2(x,y)$ and Zeeman level shift $\Delta E_{\text{Zeeman}} = \mu_B g_F^j m_F^j B_1(x,y) = \mu_j B_1(x,y)$ to the state $|j\rangle$ occur in the transverse direction. Here, α_j is the scalar polarizability of the level $|j\rangle$, and $\langle \cdots \rangle_t$ denotes the time average in an oscillating cycle, and g_F^j is the Landéfactor.

The Stark shift contributed by the far-detuned Stark field $\mathbf{E}_{\text{Stark}}$ and the Zeeman level shift contributed by the magnetic field $\mathbf{B}$ will provide the refractive index to the probe filed. The form of the refractive index will be decided by the spatial distributions of the Stark field and magnetic field. In Figure 1, $\Omega_p = (\mathbf{e}_x \cdot \mathbf{p}_{13})\mathcal{E}_p/\hbar$ and $\Omega_c = (\mathbf{e}_x \cdot \mathbf{p}_{23})\mathcal{E}_c/\hbar$ are the half Rabi frequencies of the probe and control fields, respectively. $\mathbf{p}_{ij}$ signifies the electric dipole matrix element of the transition from state $|i\rangle$ to $|j\rangle$; Δ_3 and Δ_2, are one- and two-photon detunings in the relevant transitions, respectively.

Under electric-dipole and rotating-wave approximations, the Hamiltonian reads $\hat{H}_{\text{int}} = -\hbar\sum_{j=1}^{3}\Delta_j'|j\rangle\langle j| - \hbar(\Omega_p|3\rangle\langle 1| + \Omega_c|3\rangle\langle 2| + \text{h.c.})$, where h.c. denotes the Hermitian conjugate, and $\Delta_j' = \Delta_j + \frac{\alpha_j}{2\hbar}|E_0(x,y)|^2 - \frac{\mu_j}{\hbar}B_1(x,y)$. The motion of atoms interacting with the light field is described by the time-dependent Schrödinger equation $i\hbar\frac{\partial|\psi\rangle}{\partial t} = \hat{H}_{int}|\psi\rangle$, and $|\psi\rangle = \sum_{j=1}^{3} a_j|j\rangle$. Then, we can obtain

$$\left(i\frac{\partial}{\partial t} + d_2'\right)a_2 + \Omega_c^* a_3 = 0, \tag{1}$$

$$\left(i\frac{\partial}{\partial t} + d_3'\right)a_3 + \Omega_p a_1 + \Omega_c a_2 = 0, \tag{2}$$

with $\sum_{j=1}^{3}|a_j|^2 = 1$ and $d_j' = \Delta_j' + i\gamma_j = d_j + \frac{\alpha_j}{2\hbar}|E_0(x,y)|^2 - \frac{\mu_j}{\hbar}B_1(x,y)$, a_j and γ_j are the probability amplitude and the decay rate of the states $|j\rangle$ $(j = 2, 3)$.

Under a slowly varying envelope approximation, the Maxwell equation of the probe field $\nabla^2\mathbf{E}_p - \frac{1}{c^2}\frac{\partial^2\mathbf{E}_p}{\partial t^2} = \frac{1}{c^2\varepsilon_0}\frac{\partial\mathbf{P}}{\partial t^2}$, with the polarization intensity $\mathbf{P} = a_3 a_1^*$, is reduced to

$$i\left(\frac{\partial}{\partial z} + \frac{1}{c}\frac{\partial}{\partial t}\right)\Omega_p + \frac{c}{2\omega_p}\left(\frac{\partial^2}{\partial x^2} + \frac{\partial^2}{\partial y^2}\right)\Omega_p + \kappa_{13}a_3 a_1^* = 0, \tag{3}$$

$\kappa_{13} = N\omega_p|\mathbf{e}_x \cdot \mathbf{p}_{13}|^2/(2\epsilon_0\hbar c)$ with N being the atomic concentration. Here, the slowly-variable envelope approximation $\frac{\partial\Omega_p}{\partial z} \ll ik_p\Omega_p$ and $\frac{\partial\Omega_p}{\partial t} \ll i\omega_p\Omega_p$.

We focus on steady-state regime, in which time-derivative terms in Equations (1)–(3) can be deleted. The regime can be realized by taking the probe field with a width time pulse (i.e., $|d_j|\tau_0 >> 1$, where τ_0 is the pulse length of the probe field), and hence, the response of atoms can follow the variation of the probe field adiabatically. The solutions of Equations (1) and (2) are acquired: $a_3 = d_2'\Omega_p a_1/D'$, $a_2 = -\Omega_c^*\Omega_p a_1/D'$, with $|a_1|^2 = \frac{1}{1+W'|\Omega_p|^2}$.

In general, we consider that the probe field is weaker than control field, and the Stark and Zeeman energy shifts are smaller than the detuning Δ_j. After some simple calculations, and neglecting the higher-order terms, Equation (3) is reduced into the (2 + 1) D equation with the saturable nonlinearity and trapping potential [54].

$$i\frac{\partial\Omega_p}{\partial z} + \frac{c}{2\omega_p}\nabla_\perp^2\Omega_p + \frac{\kappa_{13}d_2}{D}\frac{\Omega_p}{1+W|\Omega_p|^2} + \alpha|E_0(x,y)|^2\Omega_p + \beta B_1(x,y)\Omega_p = 0, \tag{4}$$

with $\alpha = \kappa_{13}[\alpha_2 D + d_2(\alpha_2 d_3 + \alpha_3 d_2)]/(2\hbar D^2)$, $\beta = \kappa_{13}[\mu_2 D + d_2(\mu_2 d_3 + \mu_3 d_2)]/(\hbar D^2)$, $W = (|\Omega_c|^2 + |d_2|^2)/|D|^2$, and $D = |\Omega_c|^2 - d_2 d_3$.

Equation (4) can be written into the dimensionless form

$$i\frac{\partial u}{\partial s} + (\frac{\partial^2}{\partial\xi^2} + \frac{\partial^2}{\partial\eta^2})u + \frac{c_1}{1+c_2|u|^2}u + c_3|v|^2 u + c_4 w u = 0, \tag{5}$$

where $s = z/L_{diff}$, $(\xi,\eta) = (x,y)/R_\perp$, $u = \Omega_p/U_0$, $v = E_0(x,y)/V_0$, and $w = B_0(x,y)/W_0$. With $L_{diff}(\equiv 2R_\perp^2\omega_p/c)$, $R_\perp$, U_0, V_0, and B_0 being, respectively, the characteristic diffraction length, beam radius, half Rabi frequency of the probe field, intensity of far-detuned (Stark) optical lattice field, and intensity of the magnetic field. In Equation (5), $c_1 = \kappa_{13}d_2 L_{diff}/D$, $c_2 = W{U_0}^2$, $c_3 = \alpha L_{diff}V_0^2$, and $c_4 = \beta L_{diff}W_0$.

We select the D_1 line transition $5^2S_{1/2} \longrightarrow 5^2P_{1/2}$ of the ^{87}Rb atoms. The levels, respectively, are $|1\rangle = |5S_{1/2}, F = 1, m_F = -1\rangle$, $|2\rangle = |5S_{1/2}, F = 2, m_F = -1\rangle$, and $|3\rangle = |5S_{1/2}, F = 2, m_F = -2\rangle$. Let $\gamma_1 = 0$, $\gamma_2 = 150\ \mathrm{s}^{-1}$, $\gamma_3 = 1.8 \times 10^7\ \mathrm{s}^{-1}$, $\omega_p = 2.37 \times 10^{15}\ \mathrm{s}^{-1}$, $R_\perp = 2.52 \times 10^{-3}$ cm, $\Omega_c = 6.0 \times 10^7\ \mathrm{s}^{-1}$, $\kappa_{13} = 1.0 \times 10^{11}\ \mathrm{cm}^{-1}\ \mathrm{s}^{-1}$, $\Delta_1 = 0$, $\Delta_2 = 3.6 \times 10^4 \sigma_1\ \mathrm{s}^{-1}$, $\Delta_3 = 1.0 \times 10^9\ \mathrm{s}^{-1}$, $U_0 = 6.0 \times 10^7 \sqrt{\sigma_2}\ \mathrm{s}^{-1}$, $V_0 = 380\sigma_3$ V/cm, and $W_0 = 0.09\sigma_4$ Gs. By substituting these parameters into Equation (5), we can obtain the characteristic diffraction length: $L_{diff} = 1.0$ cm.

$$c_1/\sigma_1 = 1.0 + 0.01i, c_2/\sigma_2 = 1.0, c_3/\sigma_3 = 1.0 + 0.001i, c_4/\sigma_4 = 1.0 + 0.001i. \quad (6)$$

The imaginary part of $c_i/\sigma_i (i = 1, 2, 3, 4)$ can be ignored because it is much smaller than its real part, and the dimensionless evolution equation of the probe field is obtained [54].

$$i\frac{\partial u}{\partial s} + (\frac{\partial^2}{\partial \xi^2} + \frac{\partial^2}{\partial \eta^2})u + \frac{\sigma_1}{1 + \sigma_2|u|^2}u + \sigma_3|v|^2u + \sigma_4 wu = 0. \quad (7)$$

where the values of σ_1, σ_2, σ_3, and σ_4 are individually controlled by Δ_2, U_0, V_0, and W_0. From these coefficient expressions below Equation (4), we find that σ_{1-4} relate to Δ_2, but the effect of Δ_2 on $\sigma_{2,3,4}$ can be ignored. Thus, these coefficients can be controlled individually by the system's parameters. Thus, we obtain the (2 + 1) D Equation (7) with the trapping potential, and the nonlinear coefficient and the intensity of trapping potential can be adjusted at will.

3. High-Dimensional Rogue-Wave Solutions

In this section, we discuss the high-dimensional rogue waves based on the high-dimensional NLSE (7), which is non-integrable. Modulation instability (MI) is the most familiar numerical method for exciting rogue waves, but the rogue waves excited by MI are uncontrollable. Therefore, we propose a simple and effective method of generating rogue waves. It is the split-step Fourier propagation method, which is carried out by adjusting the amplitude and width of the initial pulse. Take initial pulse as

$$u(\xi, \eta, s = 0) = C + A\exp(-\frac{\xi^2 + \eta^2}{\omega^2}). \quad (8)$$

C is the height of uniform background; A and ω are the amplitude and width of Gaussian pulse, respectively. The method has been used to generate rogue waves in low-dimensional systems [17,18]. Without losing generality, we take $C = 1$.

3.1. High-Dimensional Rogue Waves of the Kerr Nonlinear Schrödinger Equation

By taking $\Delta_2 = -1.44 \times 10^5\ \mathrm{s}^{-1}$, $U_0 \approx 4.24 \times 10^7\ \mathrm{s}^{-1}$, $V_0 = 0$ V/cm, and $W_0 = 0$ Gs, we can obtain $\sigma_1 = -4$, $\sigma_2 = 0.5$, $\sigma_3 = 0$, and $\sigma_4 = 0$. The high-dimensional Kerr NLSE,

$$i\frac{\partial u}{\partial s} + (\frac{\partial^2}{\partial \xi^2} + \frac{\partial^2}{\partial \eta^2})u + |u|^2u = 0, \quad (9)$$

is obtained by substituting parameters into Equation (7), and performing Taylor-series expansion and the phase transformation. The phase-transition regions of nonlinear modes as functions of the amplitude and width of initial pulse are shown in Figure 2a when $C = 1$. We chose some points (black points 1–2 in Figure 2a) to exhibit their propagating results. According to above criteria about shock waves, we found the red region containing point 1 for high-dimensional rogue waves, and there are only general waves in the white regions containing point 2. The profiles of nonlinear modes with different distances are shown in Figure 2b–d. We chose $\omega = 1.2$. Figure 2b is the profile of initial input pulse at $s = 0$, Figure 2c is the profile of a high-dimensional rogue wave at $s = 0.72$, and Figure 2d denotes that the high-dimensional rogue wave disappeared at $s = 1.63$. Therefore, we can control the high-dimensional rogue waves by adjusting the amplitude (A) and width (ω) of the initial pulse.

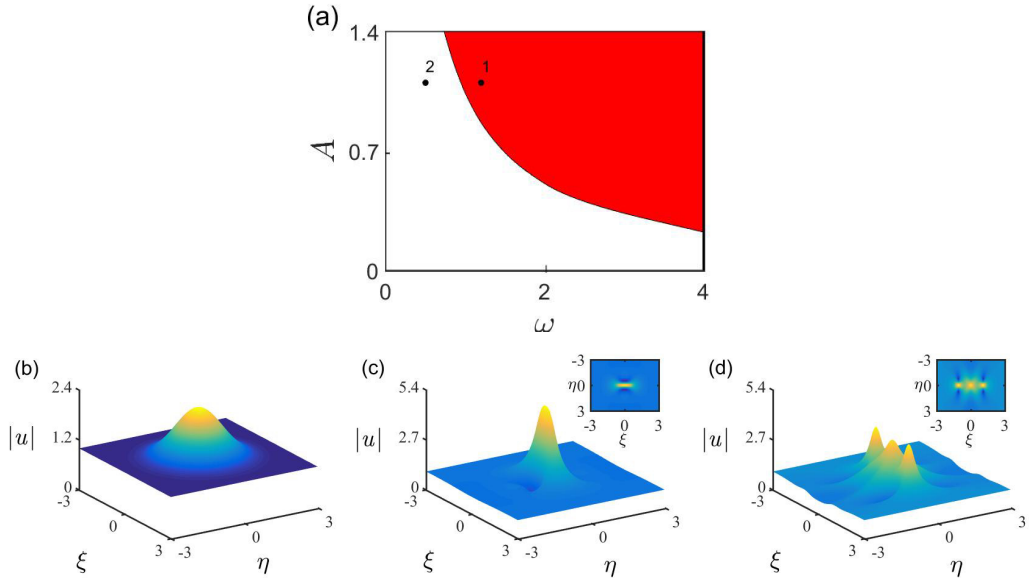

Figure 2. (Color online) (**a**) The phase transition regions of nonlinear modes as functions of amplitude (A) and width (ω) of the initial pulse when $C = 1$. According to above criteria about nonlinear modes, we found the red region containing point 1 is for high-dimensional rogue waves. (**b–d**) The profiles of nonlinear modes with different distance: $s = 0$, 0.72, and 1.63, respectively. Here, $\omega = 1.2$.

3.2. High-Dimensional Rogue Waves of the SNLSE

After choosing $\Delta_2 = -3.46 \times 10^5$ s^{-1}, $U_0 = 6.0 \times 10^7$ s^{-1}, $V_0 = 0$ V/cm, and $W_0 = 0$ Gs, $\sigma_1 = -9.6$, $\sigma_2 = 1$, $\sigma_3 = 0$, and $\sigma_4 = 0$ are obtained. Equation (7) is reduced to the high-dimensional SNLSE:

$$\mathrm{i}\frac{\partial u}{\partial s} + (\frac{\partial^2}{\partial \xi^2} + \frac{\partial^2}{\partial \eta^2})u - \frac{9.6}{1+|u|^2}u = 0, \tag{10}$$

which is non-integrable model. We can use the same method to find its rogue wave solutions.

The existence regions of nonlinear modes are shown in Figure 3a. Point 1 in Figure 3a was chosen to exhibit the propagating results. The profiles of nonlinear modes are shown in Figure 3b–d for different distances when $\omega = 1.20$. Figure 3b–d are the initial pulse at $s = 0$, the high-dimensional rogue wave at $s = 1.08$, and the disappeared state of high-dimensional rogue waves at $s = 2.00$, respectively. These results tell us that the propagation method not only can be used to generate rogue waves for NLSE (9), but also for the SNLSE (10). Both of them are non-integrable.

3.3. High-Dimensional Rogue Waves of the SNLSE with the Trapping Potential Contributed by a Far-Detuned (Stark) Optical Lattice Field

We can also take $\Delta_2 = -3.46 \times 10^5$ s^{-1}, $U_0 = 6.0 \times 10^7$ s^{-1}, $V_0 = 1.22 \times 10^3$ V/cm, and $W_0 = 0$ Gs; then, $\sigma_1 = -9.6$, $\sigma_2 = 1$, $\sigma_3 = 3.2$, and $\sigma_4 = 0$. The SNLSE

$$i\frac{\partial u}{\partial s} + (\frac{\partial^2}{\partial \xi^2} + \frac{\partial^2}{\partial \eta^2})u - \frac{9.6}{1+|u|^2}u + 3.2|v|^2 u = 0, \tag{11}$$

in which the trapping potential contributed by far-detuned (Stark) optical lattice field is derived. When $|v|^2 = \exp(-\frac{\xi^2+\eta^2}{5^2})$ is chosen, the phase-transition regions of nonlinear modes for the SNLSE (11) are shown in Figure 4a. In Figure 4b, the phase-transition curves of high-dimensional rogue waves are plotted with different values of σ_3. The blue solid line is for Equation (10), and the red dotted line is for Equation (11). The right regions of the phase-transition curves are for the rogue waves. From these, we know that the high-dimensional rogue waves can be suppressed by appropriately increasing the far-detuned electric

field. The propagation process of nonlinear modes of point 1 are shown in Figure 4c–e. Here, $\omega = 1.20$. Figure 4c is the profile of the initial pulse at $s = 0$. Figure 4d is for the high-dimensional rogue wave at $s = 0.99$, when $s = 1.61$, the rogue wave disappears, as shown in Figure 4e.

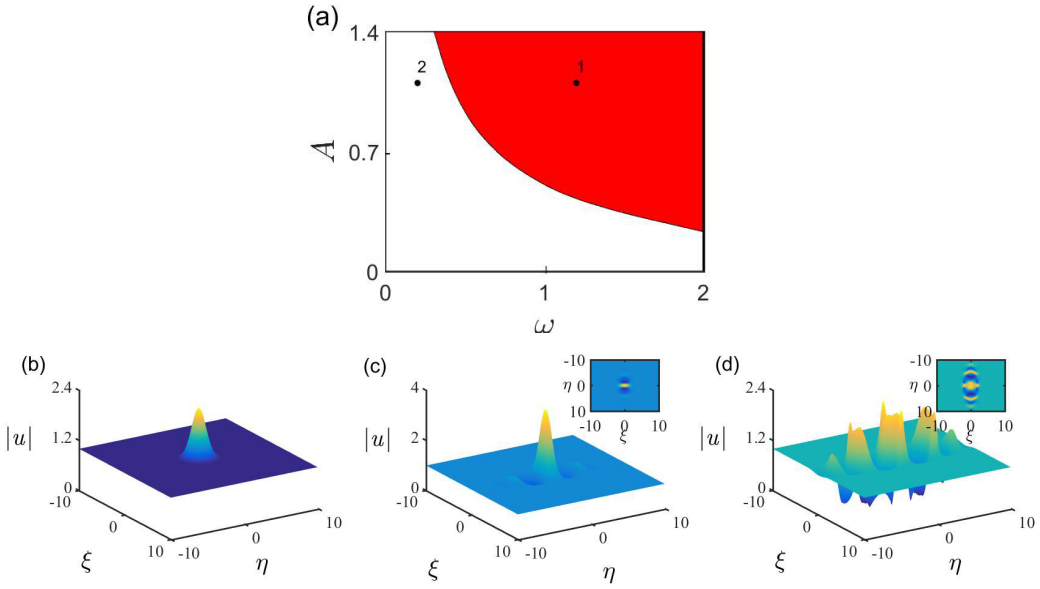

Figure 3. (Color online) (**a**) The existence regions of nonlinear modes as functions of the amplitude (A) and width (ω) of initial pulse when $C = 1$. The red region containing point 1 is for high-dimensional rogue waves. (**b**–**d**) The profiles of nonlinear modes by taking $s = 0$, 1.08, and 2.0, respectively. Here, $\omega = 1.2$.

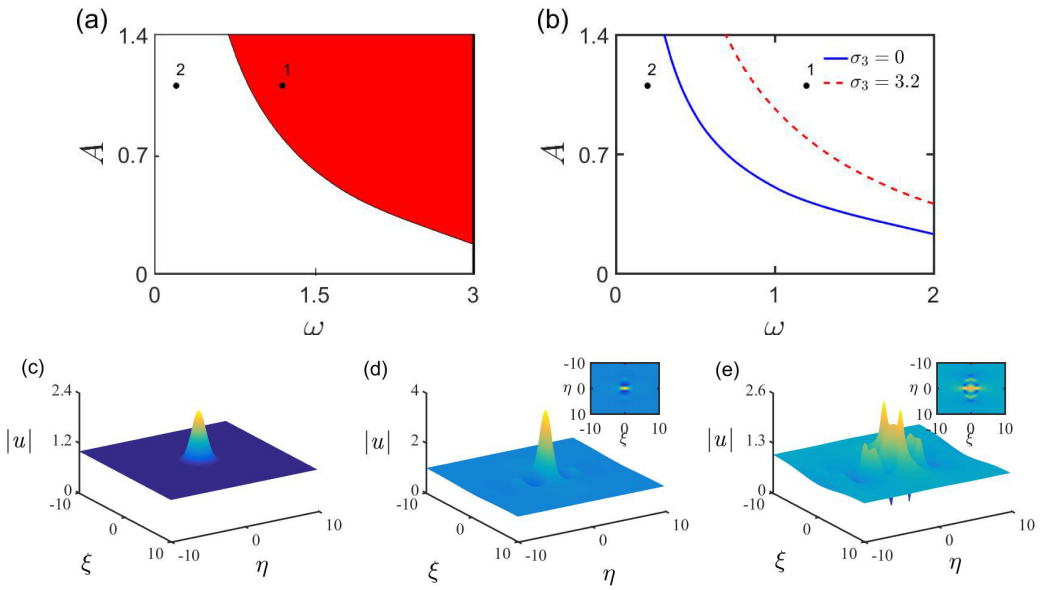

Figure 4. (Color online) (**a**) The existence regions of nonlinear modes as functions of A and ω when $C = 1$. The red region is for high-dimensional rogue waves. (**b**) The phase-transition curves of high-dimensional rogue waves for the SNLSE (11) with $\sigma_3 = 0$ (blue solid line) and 3.2 (red dotted line). The regions containing point 1 denote the existence interval of high-dimensional rogue waves. (**c**–**e**) The profiles of nonlinear modes by taking $s = 0$, 0.99, and 1.61, respectively. Here, $\omega = 1.2$.

3.4. High-Dimensional Rogue Waves of the SNLSE with a Weak Magnetic Field

Finally, $\Delta_2 = -3.46 \times 10^5$ s^{-1}, $U_0 = 6.0 \times 10^7$ s^{-1}, $V_0 = 0$ V/cm, and $W_0 = 0.36$ Gs were chosen, so $\sigma_1 = -9.6$, $\sigma_2 = 1$, $\sigma_3 = 0$, and $\sigma_4 = 4$. Equation (7) can be reduced to the SNLSE with external potential contributed by the weak magnetic field:

$$i\frac{\partial u}{\partial s} + (\frac{\partial^2}{\partial \xi^2} + \frac{\partial^2}{\partial \eta^2})u - \frac{9.6}{1+|u|^2}u + 4wu = 0. \tag{12}$$

When $w = 1 - 0.5\rho(\xi, \eta)$, and $\rho(\xi, \eta)$ are random numbers, rogue waves cannot be excited by the initial pulse. We also took other types of random potential, and this conclusion was consistent. That is, the random weak magnetic field is not conducive to the rogue waves' excitation. The reason is that rogue waves are the result of coherent resonance between waves, but random external potentials may destroy the coherence between waves, so rogue-wave generation is suppressed. Therefore, the random weak magnetic field can effectively inhibit the production of high-dimensional rogue waves, which will provide an idea for the prevention of high-dimensional freak waves, especially for the marine freak waves that could devour ships.

For when $w = \exp(-\frac{\xi^4+\eta^4}{5^4})$, the existence regions of nonlinear modes for SNLSE (12) are shown in Figure 5a. In Figure 5b, we show the phase-transition curve of the SNLSE (12) without ($\sigma_4 = 0$, blue solid line) or with ($\sigma_4 = 4.0$, red dotted line) the weak magnetic field. By comparing the phase-transition curves, we can see that the existence region of rogue waves becomes small after adding the weak magnetic field, which means it is more difficult to excite the high-dimensional rogue waves. This shows that the super-Gauss weak magnetic field is not conducive to the excitation of rogue waves. According to above criteria about nonlinear modes, we found the red region or the right regions of the phase-transition curves are for high-dimensional rogue waves. We took the parameters of point 1 to show the propagation process of rogue waves. Figure 5c is the profile of the initial pulse at $s = 0$. Figure 5d is for the profile of rogue wave at $s = 1.08$, and when $s = 1.60$, the rogue wave disappears, as shown in Figure 5e.

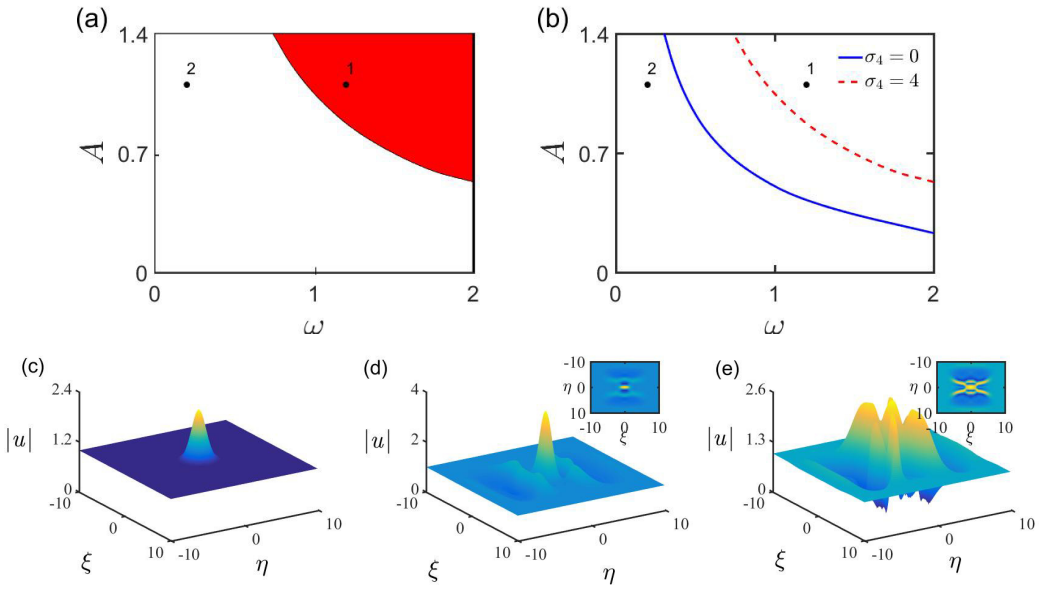

Figure 5. (Color online) (**a**) The existence regions of nonlinear modes. The red region denotes rogue waves. (**b**) The phase-transition curves of rogue waves for Equation (11) with $\sigma_4 = 0$ (blue solid line) and 4.0 (red dotted line). (**c**–**e**) The profiles of nonlinear modes when $s = 0$, 1.08, and 1.60, respectively. Here, $\omega = 1.2$.

4. Conclusions

Based on the resonant, three-level, Λ-type electromagnetically induced transparency system, the dimensionless envelope equation of the probe field was obtained. Furthermore, we were able to obtain the non-integrable, high-dimensional, nonlinear Schrödinger equations by reducing the envelope equations of the probe field, such as the Kerr-type nonlinear Schrödinger equation, SNLSE, and SNESE with external potential. By the numerical propagation method, we found their rogue-wave solutions and their existence regions in different cases. We not only proved that the numerical method can be used to find rogue-wave solutions of a non-integrable model, but also found the external potential can be used to suppress or even eliminate rogue waves. The work will not only provide a theoretical basis for experimentally controlling the high-dimensional rogue waves, but also provide an inspiration for the prevention of rogue waves disasters in the ocean. The research results also provide the ideas for excitation of rogue waves in other high-dimensional non-integrable systems.

Author Contributions: Methodology, Z.L., J.L. and H.L.; Writing—original draft, Z.L., J.L. and H.L.; Project administration, Z.L., J.L. and H.L.; Funding acquisition, Z.L., J.L. and H.L. All authors have read and agreed to the published version of the manuscript.

Funding: Project supported by Basic Scientific Research Ability of Middle-aged and Young Teachers in Colleges and Universities of Guangxi (2022KY1661, 2022KY1604), Natural Science Foundation of Zhejiang Province of China (LZ22A050002), and National Natural Science Foundation of China (11835011, 12074343).

Data Availability Statement: The original contributions presented in the study are included in the article, further inquiries can be directed to the corresponding author.

Conflicts of Interest: The authors declare no conflict of interest.

References

1. Whitemarsh, R.P. Great sea waves. *US Naval Inst. Proc.* **1934**, *60*, 1094–1103.
2. Kharif, C.; Pelinovsky, E.; Slunyaev, A. Rogue waves in the ocean. In *Rogue Waves in the Ocean;* Springer: Berlin/Heidelberg, Germany, 2009; p. 1.
3. Kharif, C.; Pelinovsky, E.; Slunyaev, A. Rogue waves in the ocean-review and progress. *EOS Trans. Am. Geophys. Union* **2010**, *91*, 104.
4. Peregrine, D.H.; Austral, J. Water waves, nonlinear Schrödinger equations and their solutions. *Math. Soc. Ser. B* **1983**, *25*, 16–43. [CrossRef]
5. Akhmediev, N.; Soto Crespo, J.M.; Ankiewicz, A. Extreme waves that appear from nowhere: On the nature of rogue waves. *Phys. Lett. A* **2009**, *373*, 2137–2145. [CrossRef]
6. Akhmediev, N.; Eleonskii, V.M.; Kulagin, N.E. Exact first-order solutions of the nonlinear Schrödinger equation. *Theor. Math. Phys.* **1987**, *72*, 809–818. [CrossRef]
7. Kharif, C.; Pelinovshy, E. Physical mechanisms of the rogue wave phenomenon. *Eur. J. Mech. B/Fluids* **2003**, *22*, 603–634. [CrossRef]
8. Onorato, M.; Residori, S.; Bortolozzo, U.; Montina, A.; Arecchi, T.F. Rogue waves and their generating mechanisms in different physical contexts. *Arecchi Phys. Rep.* **2013**, *528*, 47–89. [CrossRef]
9. Akhmediev, N.; Dudley, J.M.; Solli, D.R.; Turitsyn, S.K. Recent progress in investigating optical rogue waves (Review). *J. Opt.* **2013**, *15*, 6. [CrossRef]
10. Dudley, J.M.; Dias, F.; Erkintalo, M.; Genty, G. Instabilities, breathers and rogue waves in optics. *Nat. Photon.* **2014**, *8*, 755–764. [CrossRef]
11. Draper, L. Freak wave. *Mar. Obs.* **1965**, *35*, 193–195.
12. Kjeldsen, S.P. Dangerous wave groups. *Nor. Marit. Res.* **1984**, *12*, 4–16.
13. Diekison, D. Huge waves. In *Outside Magazine*; W. W. Norton Company: New York, NY, USA, 1995; pp. 3–5.
14. Lavernov, V. The wave energy concentration at the Agulhas current of South Affica. *Nat. Hazards* **1998**, *17*, 117–127. [CrossRef]
15. Walker, D.A.G.; Taylor, P.H.; Taylor, R.E. The shape of large surface waves on the open sea and the draupner new year wave. *Appl. Ocean Res.* **2005**, *26*, 73-83. [CrossRef]
16. Rosenthal, W.; Lehenr, S. Rogue waves: Results of the max wave project. *J. Offshore Mech. Arct. Eng.* **2008**, *130*, 021006. [CrossRef]
17. Li, Z.Y.; Li, F.F.; Li, H.J. Exciting rogue waves, breathers, and solitons in coherent atomic media. *Commun. Theor. Phys.* **2020**, *72*, 075003. [CrossRef]
18. Li, F.F.; Li, Zh.Y.; Li, H.J. Manipulating rogue waves, breathers and solitons in several non-integrable nonlinear Schrödinger equations. *Eur. Phys. J. D* **2019**, *73*, 263. [CrossRef]
19. Solli, D.R.; Ropers, C.; Koonath, P.; Jalali, B. Optical rogue waves. *Nature* **2007**, *450*, 1054–1057. [CrossRef]

20. Kibler, B.; Fatome, J.; Finot, C.; Millot, G.; Dias, F.; Genty, G.; Akhmediev, N.; Dudley, J.M. The Peregrine soliton in nonlinear fibre optics. *Nat. Phys.* **2010**, *6*, 790–795. [CrossRef]
21. Zaviyalov, A.; Egorov, O.; Iliew, R.; Lederer, F. Rogue waves in mode-locked fiber lasers. *Phys. Rev. A* **2012**, *85*, 013828. [CrossRef]
22. Manikandan, K.; Muruganandam, P.; Senthilvelan, M.; Lakshmanan, M. Manipulating matter rogue waves and breathers in Bose-Einstein condensates. *Phys. Rev. E* **2014**, *90*, 062905. [CrossRef]
23. Chen, S.H.; Baronio, F.; Soto-Crespo, J.M.; Grelu, P. Chirped Peregrine solitons in a class of cubic-quintic nonlinear Schrödinger equations. *Phys. Rev. E* **2016**, *93*, 062202. [CrossRef] [PubMed]
24. Chen, S.H.; Ye, Y.L.; Soto-Crespo, J.M.; Grelu, P.; Baronio, F. Peregrine solitons beyond the threefold limit and their two-soliton interactions. *Phys. Rev. Lett.* **2018**, *121*, 104101. [CrossRef] [PubMed]
25. Wang, X.; Liu, C.; Wang, L. Darboux transformation and rogue wave solutions for the variable-coefficients coupled Hirota equations. *J. Math. Appl.* **2017**, *449*, 1534–1552. [CrossRef]
26. Wang, X.B.; Tian, S.F.; Yan, H.; Zhang, T.T. On the solitary waves, breather waves and rogue waves to a generalized (3 + 1)-dimensional Kadomtsev-Petviashvili equation. *Math. Appl.* **2017**, *74*, 556–563. [CrossRef]
27. Wang, X.B.; Tian, Sh.F.; Qin, Ch.Y.; Zhang, T.T. Characteristics of the solitary waves and rogue waves with interaction phenomena in a generalized (3 + 1)-dimensional Kadomtsev-Petviashvili equation. *Appl. Math. Lett.* **2017**, *72*, 58–64. [CrossRef]
28. Li, M.; Shui, J.J.; Xu, T. Generation mechanism of rogue waves for the discrete nonlinear Schrödinger equation. *Appl. Math. Lett.* **2018**, *83*, 110–115. [CrossRef]
29. Wang, X.B.; Zhang, T.T.; Dong, M.J. Dynamics of the breathers and rogue waves in the higher-order nonlinear Schrödinger equation. *Appl. Math. Lett.* **2018**, *86*, 298–304. [CrossRef]
30. Zhang, X.; Chen, Y.; Tang, X. Rogue wave and a pair of resonance stripe solitons to KP equation. *Comput. Math. Appl.* **2018**, *76*, 1938–1949. [CrossRef]
31. Jia, R.R.; Guo, R. Breather and rogue wave solutions for the (2 + 1)-dimensional nonlinear Schrödinger-Maxwell-Bloch equation. *Appl. Math. Lett.* **2019**, *93*, 117–123. [CrossRef]
32. Chen, S.; Yan, Z. The Hirota equation: Darboux transform of the Riemann-Hilbert problem and higher-order rogue waves. *Appl. Math. Lett.* **2019**, *95*, 65–71. [CrossRef]
33. Yang, B.; Yang, J.K. On general rogue waves in the parity-time-symmetric nonlinear Schrödinger equation. *J. Math. Anal. Appl.* **2020**, *487*, 124023. [CrossRef]
34. Banik, S.; Shikha, R.K.; Noman, A.A.; Chowdhury, N.A.; Mannan, A.; Roy, T.S.; Mamun, A.A. First and second-order dust-ion-acoustic rogue waves in non-thermal plasma. *Eur. Phys. J. D* **2021**, *75*, 43. [CrossRef]
35. Mohammadnejad, M.; Akbari-Moghanjughi, M. Formation of ion acoustic rogue waves in warm dense matter. *Eur. Phys. J. D* **2021**, *75*, 307. [CrossRef]
36. Talouneh, K.; Kheradmand, R.; Tissoni, G.; Eslami, M. Influence of transverse carrier diffusion on two-dimensional optical rogue waves in broad-area semiconductor lasers with a saturable absorber. *Phys. Rev. A* **2022**, *105*, 013501. [CrossRef]
37. Cheng, D.; Wang, W.W.; Pan, C.C.; Hou, C.; Chen, Sh.H.; Mihalache, D.; Baronio, F. Photonic rogue waves in a strongly dispersive coupled-cavity array involving self-attractive Kerr nonlinearity. *Phys. Rev. A* **2022**, *105*, 013717. [CrossRef]
38. Ablowitz, M.J.; Davide, T.C. Transverse instability of rogue waves. *Phys. Rev. Lett.* **2021**, *127*, 104101. [CrossRef]
39. Marcucci, G.; Kheradmand, P.; Claudio, C. Theory of neuromorphic computing by waves: Machine learning by rogue waves, dispersive shocks, and solitons. *Phys. Rev. A* **2020**, *125*, 093901. [CrossRef]
40. Asgarnezhad-Zorgabad, S.; Sadighi-Bonabi, R.; Kibler, B.; Ozdemir, S.K.; Sanders, B.C. Surface-polaritonic phase singularities and multimode polaritonic frequency combs via dark rogue-wave excitation in hybrid plasmonic waveguide. *New J. Phys.* **2020**, *22*, 033008. [CrossRef]
41. Tan, Y.C.; Bai, X.D.; Li, T.T. Super rogue waves: Collision of rogue waves in Bose-Einstein condensate. *Phys. Rev. E* **2022**, *106*, 014208. [CrossRef]
42. Tlidi, M.; Taki, M. Rogue waves in nonlinear optics. *Adv. Opt. Photonics* **2022**, *14*, 87–147. [CrossRef]
43. Copus, M.G.; Camley, R.E. Creation of magnetic rogue waves. *Phys. Rev. B* **2020**, *102*, 220410. [CrossRef]
44. Ankiewicz, A.; Chowdury, A. Analysis of characteristics of rogue waves for higher-order equations. *Nonlinear Dyn.* **2022**, *22*, 07497. [CrossRef]
45. Sgrignuoli, F.; Chen, Y.; Gorsky, S.; Britton, W.A.; Negro, L.D. Optical rogue waves in multifractal photonic arrays. *Phys. Rev. B* **2021**, *103*, 195403. [CrossRef]
46. Gatz, S.; Herrmann, J. Soliton propagation in materials with saturable nonlinearity. *J. Opt. Soc. Am. B* **1991**, *8*, 2296. [CrossRef]
47. Gatz, S.; Herrmann, J. Soliton propagation and soliton collision in double-doped fibers with a non-Kerr-like nonlinear refractive-index change. *Opt. Lett.* **1992**, *17*, 484. [CrossRef]
48. Herrmann, J. Propagation of ultrashort light pulses in fibers with saturable nonlinearity in the normal-dispersion region. *J. Opt. Soc. Am. B* **1991**, *8*, 1507–1511. [CrossRef]
49. Krolikowski, W.; Luther-Davies, B. Analytic solution for soliton propagation in a nonlinear saturable medium. *Opt. Lett.* **1992**, *17*, 1414. [CrossRef]
50. Jakubowski, M.H.; Steiglitz, K.; Squier, R. Information transfer between solitary waves in the saturable Schrödinger equation. *Phys. Rev. E* **1997**, *56*, 7267. [CrossRef]

51. Melvin, T.R.; Champneys, A.R.; Kevrekidis, P.G.; Cuevas, J. Radiationless traveling waves in saturable nonlinear Schrödinger lattices. *Phys. Rev. Lett.* **2006**, *97*, 124101. [CrossRef]
52. Chen, G.; Ma, S. Ground state and geometrically distinct solitons of discrete nonlinear Schrödinger equations with saturable nonlinearities. *Stud. Appl. Math.* **2013**, *131*, 389. [CrossRef]
53. Krolikowski, W.; Luther-Davies, B. Dark optical solitons in saturable nonlinear media. *Opt. Lett.* **1993**, *18*, 188. [CrossRef]
54. Zhang, K.; Liang, Y.Z.; Lin, J.; Li, H.J. Controlling the stability of nonlinear optical modes via electromagnetically induced transparency. *Phys. Rev. A* **2018**, *97*, 023844. [CrossRef]
55. Li, H.J.; Dong, L.W.; Hang, C.; Huang, G.X. Gain-assisted high-dimensional self-trapped laser beams at very low light levels. *Phys. Rev. A* **2011**, *83*, 023816. [CrossRef]
56. Schmidt, H.; Imamoglu, A. Giant Kerr nonlinearities obtained by electromagnetically induced transparency. *Opt. Lett.* **1996**, *21*, 1936–1938. [CrossRef]
57. Harris, S.E. Electromagnetically induced transparency. *Phys. Today* **1997**, *50*, 36–42. [CrossRef]
58. Hau, L.V.; Harris, S.E.; Dutton, Z.; Behroozi, C.H. Light speed reduction to 17 metres per second in an ultracold atomic gas. *Nature* **1999**, *397*, 594–598. [CrossRef]
59. Li, H.J.; Wu, Y.P.; Hang, C.; Huang, G.X. (3 + 1)-dimensional superluminal spatiotemporal optical solitons and vortices at weak light level. *Phys. Rev. A* **2012**, *86*, 25181–25194. [CrossRef]
60. Liu, J.Y.; Hang, C.; Huang, G.X. Weak-light rogue waves, breathers, and their active control in a cold atomic gas via electromagnetically induced transparency. *Phys. Rev. A* **2016**, *93*, 063836. [CrossRef]
61. Liu, J.Y.; Hang, C.; Huang, G.X. Weak-light vector rogue waves, breathers, and their Stern-Gerlach deflection via electromagnetically induced transparency. *Opt. Express* **2017**, *25*, 23408–23423. [CrossRef]